

A deep learning approach to predict thermophysical properties of metastable liquid Ti-Ni-Cr-Al alloy

Cite as: J. Appl. Phys. 133, 085102 (2023); doi: 10.1063/5.0138001

Submitted: 20 December 2022 · Accepted: 8 February 2023 ·

Published Online: 22 February 2023



R. L. Xiao,¹  Q. Wang,¹  J. Y. Qin,²  J. F. Zhao,¹  Y. Ruan,^{1,a)}  H. P. Wang,¹  H. Li,² and B. Wei¹ 

AFFILIATIONS

¹MOE Key Laboratory of Materials Physics and Chemistry under Extraordinary Conditions, School of Physical Science and Technology, Northwestern Polytechnical University, Xi'an 710072, China

²Key Laboratory for Liquid-Solid Structural Evolution and Processing of Materials, Ministry of Education, Shandong University, Jinan 250061, China

^{a)}Author to whom correspondence should be addressed: ruany@nwpu.edu.cn

ABSTRACT

The physical properties of liquid alloy are crucial for many science fields. However, acquiring these properties remains challenging. By means of the deep neural network (DNN), here we presented a deep learning interatomic potential for the Ti-Ni-Cr-Al liquid system. Meanwhile, the thermophysical properties of the Ti-Ni-Cr-Al liquid alloy were experimentally measured by electrostatic levitation and electromagnetic levitation technologies. The DNN potential predicted this liquid system accurately in terms of both atomic structures and thermophysical properties, and the results were in agreement with the *ab initio* molecular dynamics calculation and the experimental values. A further study on local structure carried out by Voronoi polyhedron analysis showed that the cluster exhibited a tendency to transform into high-coordinated cluster with a decrease in the temperature, indicating the enhancement of local structure stability. This eventually contributed to the linear increase in the density and surface tension, and the exponential variation in the viscosity and the diffusion coefficient with the rise of undercooling.

Published under an exclusive license by AIP Publishing. <https://doi.org/10.1063/5.0138001>

INTRODUCTION

The information on thermophysical properties and structure evolution of liquid substances are of vital importance in the fields of materials science, condensed matter physics, engineering thermophysics, etc.^{1–4} Containerless processing methods represented by electrostatic levitation and electromagnetic levitation were applied to measure the thermophysical properties and determine the liquid structure of alloy melt.^{5–7} However, the volatilization caused by high saturated vapor pressure in an overheated state, and the disturbance for the undercooled state from the oscillation during the measurements hindered the experimental measurement of the parameters in a wide temperature range. The molecular simulation can solve this problem, whereas the molecular simulation is faced with the dilemma of accuracy vs efficiency.^{8–10} The *ab initio* molecular dynamics (AIMD) based on quantum mechanics and density-functional theory (DFT) is an accurate description of the

dynamic behavior of systems. However, the computation is expensive and has a finite range of spatial and temporal scales (500 atoms and 1 ns). The classic molecular dynamics (MD) based on empirical force fields allows a larger system and longer time scale, whereas MD is of somewhat worse accuracy and transferability compared with AIMD. Moreover, the force fields in classic MD for multicomponent systems are complicated and tedious.¹¹

Benefiting from the development of machine learning methods, the deep potential molecular dynamics based on the deep neural network (DNN) algorithm implemented by DeePMD-kit is becoming a new powerful method for addressing the above problems.^{9–14} For metallic materials, the DeePMD-kit interfaces with TensorFlow and Large-scale Atomic/Molecular Massively Parallel Simulator (LAMMPS) give the accurate estimation of solid lattice parameters,^{15,16} density of the unary and binary system,^{12,15,17} liquid structure evolution,^{8,12,15} melting and solidification behaviors,^{8,15,17} and mechanical response.¹⁶ Here, to conquer the disadvantages such as

the absence of empirical force fields for classic MD simulation, the finite range of spatial and temporal scales for AIMD simulation, and the limited temperature range for experiment measurements, we proposed a machine learning method to accurately estimate the liquid thermophysical properties of a multicomponent system.

In this work, the thermophysical properties and liquid structure of quaternary $\text{Ti}_{79}\text{Ni}_{10}\text{Cr}_6\text{Al}_5$ alloy melt were studied by deep learning methods, electrostatic levitation (ESL) and electromagnetic levitation (EML) techniques. The DNN potential for a molten Ti–Ni–Cr–Al alloy was developed. The density, surface tension, and viscosity were achieved by calculation based on DNN potential and experimentally measured by ESL and EML for comparison. Besides, the liquid structure and diffusion coefficient were acquired in a broader temperature range by utilizing the DNN potential in DeePMD-kit, and the relationship between local structure and thermophysical properties was discussed.

METHODS

The training datasets for DNN potential were generated by AIMD in Vienna *Ab initio* Simulation Program (VASP).¹⁸ The projector augmented-wave (PAW) pseudopotentials and Perdew–Burke–Ernzerhof (PBE) gradient approximation to the exchange–correlation functional were adopted to describe the atom interaction. The $\text{Ti}_{79}\text{Ni}_{10}\text{Cr}_6\text{Al}_5$ alloy melt system contained 200 particles. Only the Γ point was used to sample the Brillouin zone, and the energy cutoff of 300 eV was set. The time step was 3 fs. The AIMD simulations were performed using the periodic boundary conditions and canonical (NVT) ensemble with the Nosé–Hoover thermostat. The simulation temperatures were chosen to be 2500, 2100, 1700, 1400, and 1200 K. The cubic box was adjusted to keep the external pressure in the range of 0 ± 1 kbar. At each temperature, the system was run for 20 000 steps where 18 000 steps were used as training and another 2000 steps were used as validation. Moreover, 5000 steps of simulation for $\text{Ti}_{70}\text{Ni}_{10}\text{Cr}_{10}\text{Al}_{10}$ and $\text{Ti}_{40}\text{Ni}_{20}\text{Cr}_{20}\text{Al}_{20}$ alloy melt systems at 2500, 1850, and 1200 K were added into the training data to improve the accuracy of DNN potential.

The DeePMD-kit was used for the training of DNN potential.¹¹ Compared with the other machine learning methods, the deep learning exhibited a better performance in dealing with plentiful datasets from AIMD with extensive and symmetry-invariant properties. The model based on the assumption that the energy of the system consisting of N atoms can be counted from every single atom which can be expressed as

$$E = \sum_i E_i. \quad (1)$$

The atomic energy E_i of atom i depends on the local atomic configuration. For the j atom, the distance of which from i is less than the cutoff radius, the local atomic configuration for i is parametrized by the descriptor matrix,

$$D_{ij}^\alpha = \left\{ \frac{1}{R_{ij}}, \frac{x_{ij}}{R_{ij}}, \frac{y_{ij}}{R_{ij}}, \frac{z_{ij}}{R_{ij}} \right\}, \quad (2)$$

where R_{ij} is the distance between i and j , and x_{ij} , y_{ij} , and z_{ij} are the

relative coordinates. In addition, the atomic energy of i can be expressed as

$$E_i = \mathcal{N}_{(i)}(D_{ij}^\alpha), \quad (3)$$

where \mathcal{N} is the multilayer perceptron with the hidden layer. The cutoff radius was 6 Å, and the smooth started from 5.8 Å. The force F_i on the atom i and virial Ξ of the system are given by the following equations:

$$\begin{aligned} F_i = & - \sum_{j \in N(i), \alpha} \frac{\partial \mathcal{N}_{(i)}}{\partial D_{ij}^\alpha} \frac{\partial D_{ij}^\alpha}{\partial R_i} - \sum_{j \neq i} \sum_{k \in N(j), \alpha} \delta_{i, a(j)} \frac{\partial \mathcal{N}_{(j)}}{\partial D_{jk}^\alpha} \frac{\partial D_{jk}^\alpha}{\partial R_i} \\ & - \sum_{j \neq i} \sum_{k \in N(j), \alpha} \delta_{i, b(j)} \frac{\partial \mathcal{N}_{(j)}}{\partial D_{jk}^\alpha} \frac{\partial D_{jk}^\alpha}{\partial R_i} \\ & - \sum_{j \neq i} \sum_{k \in N(j), \alpha} \delta_{i, k} \frac{\partial \mathcal{N}_{(j)}}{\partial D_{jk}^\alpha} \frac{\partial D_{jk}^\alpha}{\partial R_i}, \end{aligned} \quad (4)$$

$$\Xi = - \sum_{i \neq j} R_{ij} \sum_{\alpha} \frac{\partial \mathcal{N}_{(i)}}{\partial D_{ij}^\alpha} \frac{\partial D_{ij}^\alpha}{\partial R_{ij}} - \sum_{i \neq j} \delta_{j, a(i)} R_{ij} \sum_{q, \alpha} \frac{\partial \mathcal{N}_{(i)}}{\partial D_{iq}^\alpha} \frac{\partial D_{iq}^\alpha}{\partial R_{ij}}, \quad (5)$$

where R_i is the position of i and $N(i)$ is the neighbor list of i . The loss function L is defined as

$$L = \frac{p_\epsilon}{N} \Delta E^2 + \frac{p_f}{3N} \sum_i |\Delta F_i|^2 + \frac{p_\xi}{9N} \|\Delta \Xi\|^2, \quad (6)$$

where ΔE , ΔF_i , and $\Delta \Xi$ are the root mean square (RMS) errors and p_ϵ , p_f , and p_ξ are the prefactors of energy, force, and virial, respectively. In the training, the numbers of the embedding and fitting net were (25, 50, 100) and (240, 240, 240), respectively. 5×10^6 epochs with an exponentially decaying learning rate from 1.00×10^{-3} to 3.51×10^{-8} were trained in a NVIDIA TESLA V100 TENSOR CORE GPU. After the DNN potential was generated, the MD simulation was carried out by LAMMPS.¹⁹

The ESL⁶ and the EML²⁰ experiments were carried out for evaluating the DNN potential. The $\text{Ti}_{79}\text{Ni}_{10}\text{Cr}_6\text{Al}_5$ alloy was prepared from pure Ti (99.999%), pure Ni (99.999%), pure Cr (99.999%), and pure Al (99.999%) in an arc melting furnace. In the ESL experiments, an alloy sample with a diameter of about 2.5 mm was levitated in the 10^{-4} Pa vacuum environment. The ESL sample temperature was monitored by a Sensortherm GmbH M322 pyrometer. The density was measured by detecting the sample image evolution using the high-resolution CCD camera, which was calibrated by levitating a standard steel ball of precisely known diameter. The samples under the ESL condition can reach a high undercooling level, which was an asset in measuring thermophysical properties of a metastable state, but the volatilization led by overheating degree should be noticed. In the EML experiments, the chamber was first pumped to a high vacuum environment (10^{-4} Pa) and then backfilled with a mixture gas of high purity Ar (99.999%), He (99.999%), and H_2 (99.999%) in the volume rate of 10:9:1 avoiding oxidation. The EML sample temperature was monitored by a KELLER CellaTemp PA20 pyrometer. The EML samples

had less volatilization under the overheating condition in the protective atmosphere, whereas the samples had difficulties in getting undercool, compared with ESL samples. Thus, for the purposes of higher data reliability and border data range, the surface tension was determined on both ESL and EML facilities by the oscillating drop method.^{6,20}

RESULTS AND DISCUSSION

Figures 1(a)–1(c) show the energy, force, and virial calculated by AIMD and DNN potential, respectively. The predicted energy, force, and virial of training data by DNN potential were close to the *ab initio* result. For the validation data that are not included in the training data, randomly 200 configurations were used to test the DNN potential. The predicted energy, force, and virial of validation data exhibited linear correlations and were also close to the *ab initio* result. The 10^{-3} , 10^{-1} , and 10^{-2} order RMS errors in predicted energy, force, and virial of validation data, respectively, indicate that the DNN potential accurately reproduced the *ab initio* results.

To further verify the DNN potential and investigate the liquid structure evolution, the pair distribution function (PDF) of liquid alloy and the partial PDFs of several different pair atoms at each training temperature were calculated and shown in Figs. 2(a) and 2(b). The PDFs and partial PDFs calculated from DNN potential were in accord with the AIMD results. Thus, the developed DNN potential reproduced well the average liquid structure in the range of 1200–2500 K compared with the AIMD simulations.

The structural characteristics of the liquid $\text{Ti}_{79}\text{Ni}_{10}\text{Cr}_6\text{Al}_5$ alloy are summarized in Fig. 2(b). The height of the first and second peaks for Ti–Ti, Ti–Ni, Ti–Al, Ti–Cr, Ni–Ni, Ni–Al, Al–Cr, and Cr–Cr partial PDFs increased with the cooling period, suggesting the above atoms tended to bond with each other. The height of the first peak for Al–Al and Ni–Cr partial PDFs decreased with the decreasing temperature. This meant that the Al–Al and Ni–Cr bonds were not inclined to form. Moreover, the intensities of the second peak for Ni–Cr, Ni–Ni, and the undercooled Al–Al partial PDFs were stronger than those of the first peak. This demonstrated

that the intermediate range order dominated the local structure of Ni and Cr atoms around Ni atoms and Al around Al atoms.

As we introduced above, the thermophysical properties are important fundamental parameters in many fields. Based on the DNN potential, the density, surface tension, viscosity, and diffusion coefficients including a deep undercooling region and a large overheating region were calculated, as shown in Figs. 3(a)–3(d). In the MD simulation, the surface tension σ was calculated by the following equation:²¹

$$\sigma = \frac{V}{2A} \left\langle P_{zz} - \frac{1}{2}(P_{xx} + P_{yy}) \right\rangle, \quad (7)$$

where V is the volume; A is the area of liquid–vapor interface; P_{xx} , P_{yy} , and P_{zz} are the tangential components of the pressure tensor. The viscosity η can be calculated by the following Green–Kubo equation:²²

$$\eta = \frac{V}{Nk_B T} \int_0^\infty \langle P_i(t)P_i(0) \rangle dt, \quad (8)$$

where k_B is the Boltzmann constant ($1.38 \times 10^{-23} \text{ J K}^{-1}$) and $P_i(t)$ represents the off-diagonal components of the atomic stress tensor at time t . The diffusion coefficient D was derived from the relationship between the diffusion coefficient and mean square displacement,

$$D = \lim_{t \rightarrow \infty} \frac{1}{6N} \frac{\partial}{\partial t} \sum_{i=1}^N \langle |r_i(t) - r_i(0)|^2 \rangle, \quad (9)$$

where r_i is the position of the atom i .

The calculated density, surface tension, viscosity, and diffusion coefficients changed continuously and fluctuated slightly, even at the temperatures not involved in the AIMD calculation, implying the remarkable temperature transformability of the DNN potential. The density and surface tension calculated by DNN potential

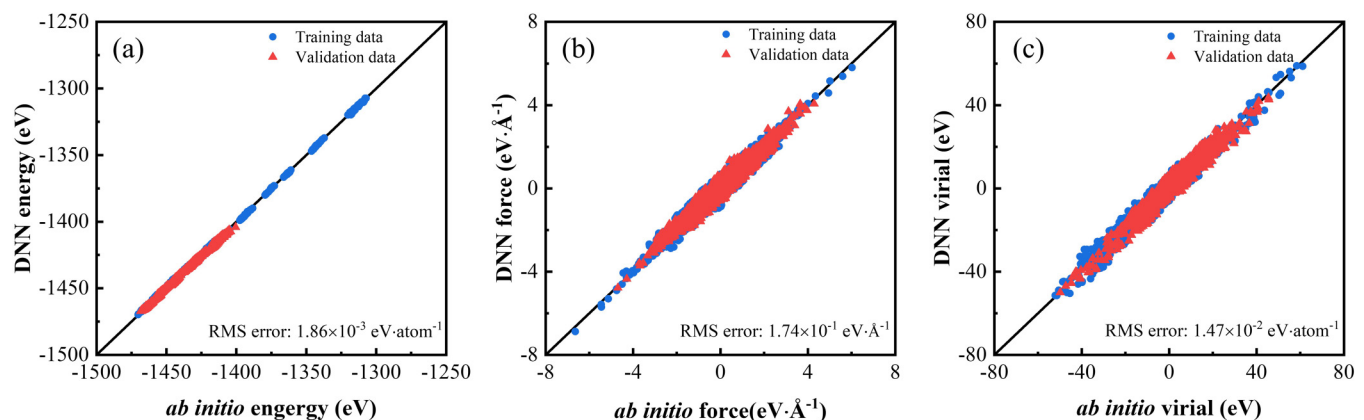


FIG. 1. Correlations between AIMD and DNN data: (a) energy, (b) force, and (c) virial.

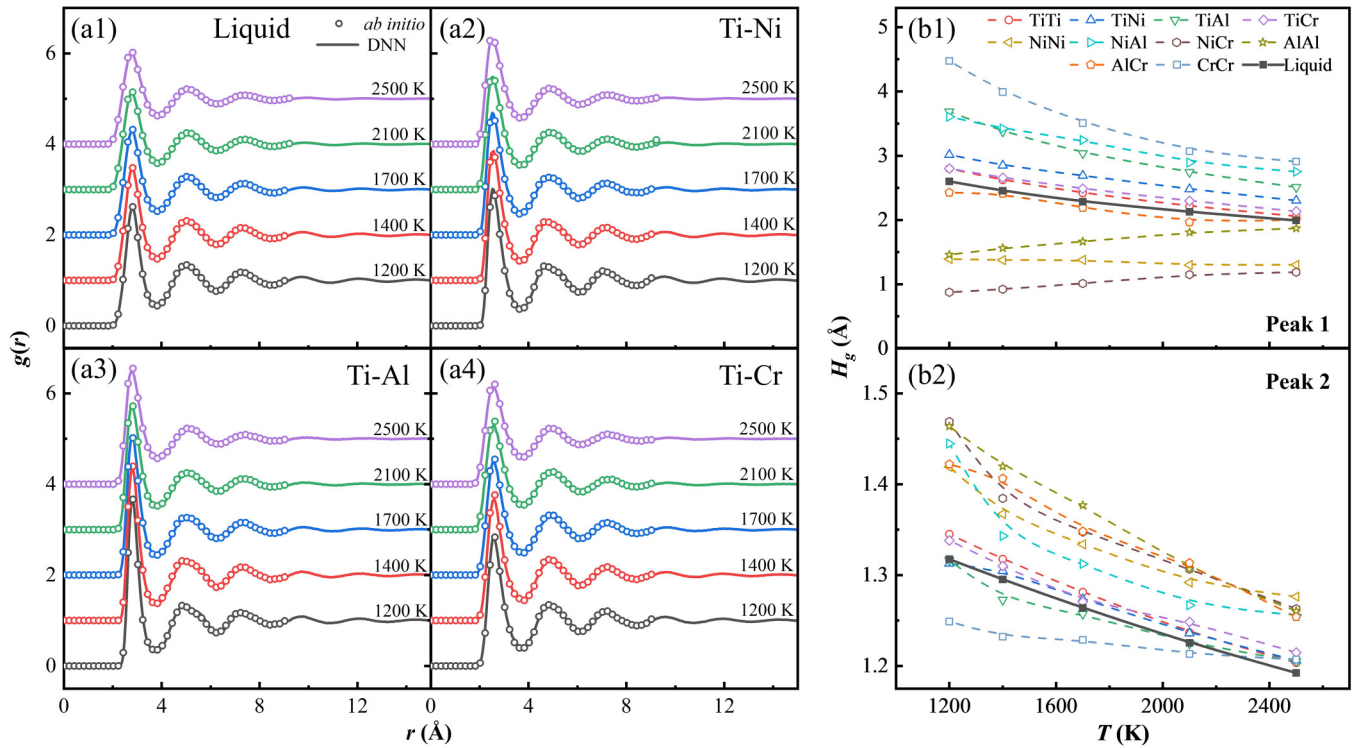


FIG. 2. Liquid structural characteristics of the $\text{Ti}_{79}\text{Ni}_{10}\text{Cr}_6\text{Al}_5$ alloy at different temperatures: (a) PDF of liquid alloy and partial PDF of different pair atoms, (b) height of the PDF peaks.

accorded closely with the experiment results. The difference between the calculated density and ESL experiment value (uncertainty 0.68%) at T_L point was less than 0.2%. The calculated surface tension values exhibited an error less than 3% with the EML results (uncertainty 1.24%) in the whole temperature range and 4%–6% with ESL values (uncertainty 1.53%) in the undercooling range. The surface tension values in the overheating range achieved by EML were more precise than those measured by ESL because the latter was sensitive to the high temperature volatilization. Moreover, the viscosity of pure Ti²³ and the values derived from the measured surface tension by the Egry model²⁴ were listed in Fig. 3(c). The viscosity calculated by DNN potential was also well consistent with the reference data. The very narrow differences between the calculated values and experiment results indicated the high accuracy of the trained DNN potential for the $\text{Ti}_{79}\text{Ni}_{10}\text{Cr}_6\text{Al}_5$ melt.

The density and surface tension of $\text{Ti}_{79}\text{Ni}_{10}\text{Cr}_6\text{Al}_5$ melt exhibited a linear temperature dependence. They both increased with the decreasing temperature. The densities of the liquid alloy were fitted as follows:

$$\rho_{\text{DNN}} = 4.62 - 2.12 \times 10^{-4}(T - T_L), \quad (10)$$

$$\rho_{\text{ESL}} = 4.61 - 2.71 \times 10^{-4}(T - T_L). \quad (11)$$

The surface tension of the liquid alloy can be expressed as

$$\sigma_{\text{DNN}} = 1.65 - 1.58 \times 10^{-4}(T - T_L), \quad (12)$$

$$\sigma_{\text{EML}} = 1.62 - 2.16 \times 10^{-4}(T - T_L), \quad (13)$$

$$\sigma_{\text{ESL}} = 1.54 - 4.22 \times 10^{-4}(T - T_L). \quad (14)$$

The temperature dependence of the viscosity and the diffusion coefficients of different components were well described by the following Arrhenius relationship:

$$\eta_{\text{DNN}} = 0.30 \exp\left(\frac{3.61 \times 10^4}{R_g T}\right), \quad (15)$$

$$D_L = 9.39 \times 10^{-8} \exp\left(\frac{-4.54 \times 10^4}{R_g T}\right), \quad (16)$$

$$D_{\text{Ti}} = 9.14 \times 10^{-8} \exp\left(\frac{-4.54 \times 10^4}{R_g T}\right), \quad (17)$$

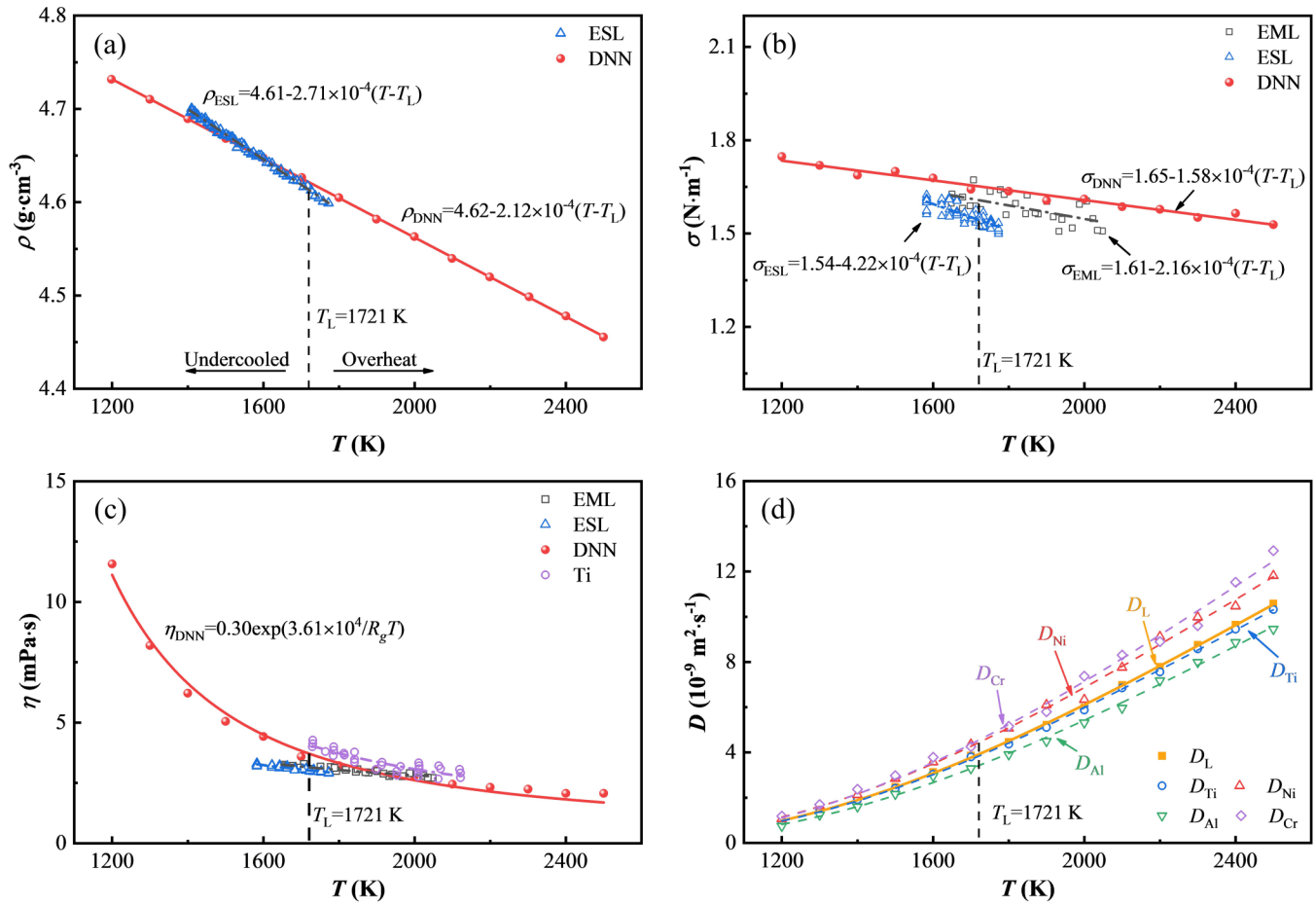


FIG. 3. Thermophysical properties of the liquid $\text{Ti}_{79}\text{Ni}_{10}\text{Cr}_6\text{Al}_5$ alloy: (a) density, (b) surface tension, (c) viscosity, and (d) diffusion coefficient.

$$D_{\text{Ni}} = 1.02 \times 10^{-7} \exp\left(\frac{-4.48 \times 10^4}{R_g T}\right), \quad (18)$$

$$D_{\text{Cr}} = 1.16 \times 10^{-7} \exp\left(\frac{-4.63 \times 10^4}{R_g T}\right), \quad (19)$$

$$D_{\text{Al}} = 9.28 \times 10^{-8} \exp\left(\frac{-4.72 \times 10^4}{R_g T}\right), \quad (20)$$

where R_g is the ideal gas constant ($8.314 \text{ J mol}^{-1} \text{ K}^{-1}$). Since Ti is the major element of the alloy, the D - T curve of the liquid alloy is reasonably similar to that of Ti. The Cr and Ni atoms have faster diffusion rates because of their smaller atomic radius. These thermophysical parameters were determined and influenced by the local structure of the liquid alloy.

The Voronoi polyhedron (VP) analysis was hired to provide more information on the local topological structure of the liquid

alloy.^{25,26} The Voronoi index $\langle n_3, n_4, n_i, \dots \rangle$ was used to describe the types of Voronoi cells (VCs), where n_i is the number of i -edged faces. The sum of n_i is equivalent to the coordination number (CN) of the central atom. The fraction of 15 most abundant VCs in the liquid alloy and CNs of different central atoms were counted and presented in Figs. 4(a) and 4(b). The fraction of the ICO cluster $\langle 0, 0, 12, 0 \rangle$ and distorted ICO clusters $\langle 0, 2, 8, 2 \rangle$ and $\langle 0, 1, 10, 2 \rangle$ increased with the decreasing temperature. The clusters with CN = 13 were dominated by Ti centers. It is interesting to note that the higher CN cluster will replace the smaller CN cluster in Ni (CN = 11 \rightarrow 12), Cr (CN = 11 \rightarrow 12), and Al (CN = 12 \rightarrow 13) centered clusters and transform into a dominant cluster, once the temperature decreases below the threshold. Moreover, the relatively high-coordinated cluster (solid symbol and full line) increased and the low-coordinated cluster (hollow symbol and dash line) decreased with decreasing temperature for all kinds of central atoms, indicating that the clusters with loose correlation transformed into tight correlation clusters. This enhanced the local structure stability, decreased the system potential energy, and

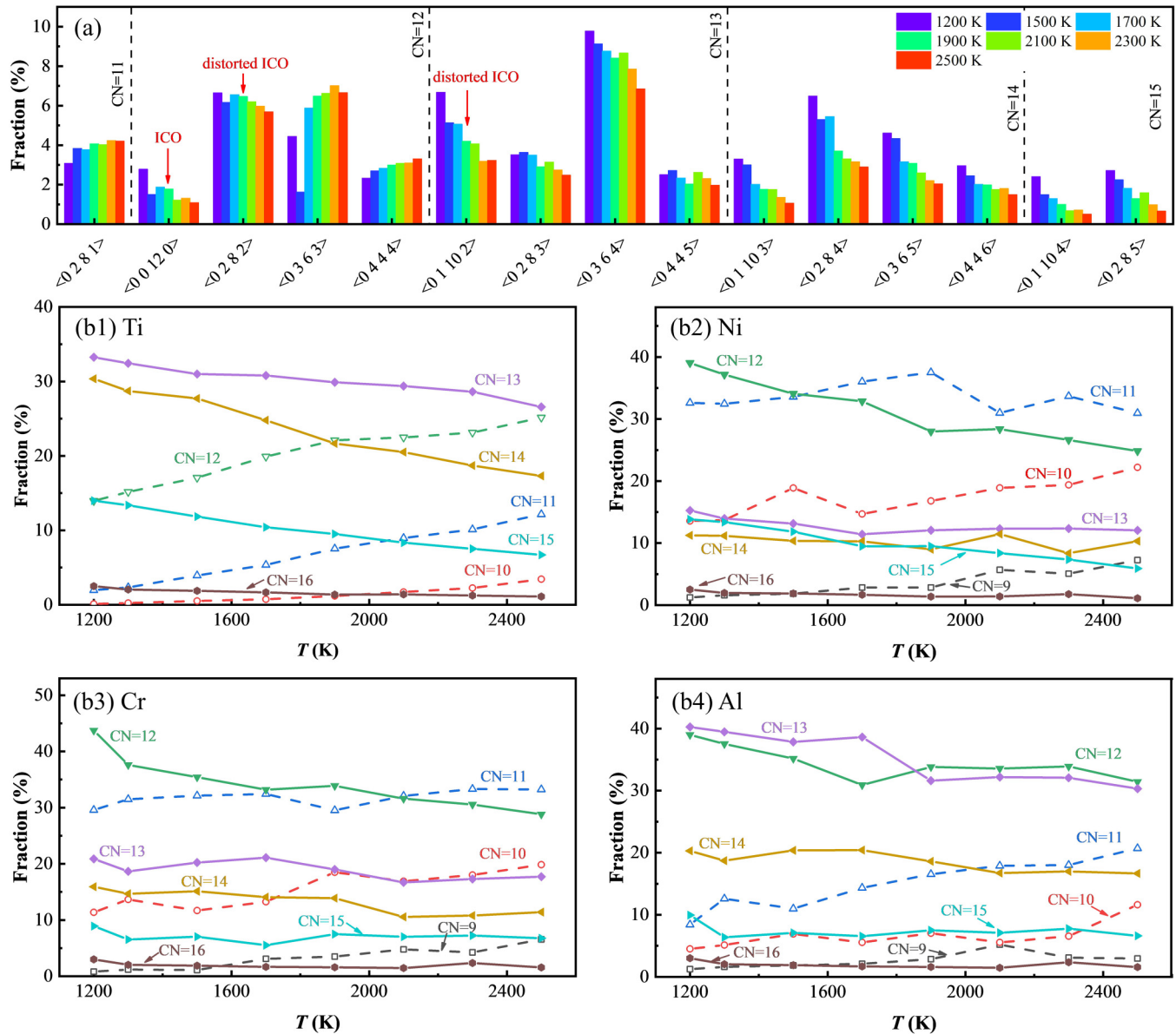


FIG. 4. VP analysis for the liquid $\text{Ti}_{79}\text{Ni}_{10}\text{Cr}_6\text{Al}_5$ alloy: (a) fraction of VCs in liquid and fraction of CNs for (b1) Ti, (b2) Ni, (b3) Cr, and (b4) Al central atoms, respectively.

subsequently influenced thermophysical properties, i.e., increased the density and surface tension and decreased atomic diffusion ability.

CONCLUSIONS

In summary, we developed a DNN potential for the liquid $\text{Ti}_{79}\text{Ni}_{10}\text{Cr}_6\text{Al}_5$ alloy by means of deep learning. This DNN potential described the average atomic distribution well compared with AIMD simulation, and the calculated thermophysical property

parameters were in well accord with the measured values by ESL and EML techniques, demonstrating the high accuracy and good temperature transformability of the DNN potential. The temperature dependence of the density calculated by the DNN potential was $\rho = 4.62 - 2.12 \times 10^{-4}(T - T_L)$. The surface tension and viscosity at T_L were 1.65 N m^{-1} and 3.74 mPa s , respectively. The VP analysis indicated that a large amount of ICO and distorted ICO clusters were formed with a decrease in the temperature. Moreover, based on the temperature dependency of CNs of different central atoms, the clusters were inclined to convert into high-coordinated

clusters. This clustering behavior was essential to the decrease in the potential energy and the enhancement of local structure stability, consequently resulting in the variation in the thermophysical parameters of the liquid alloy.

ACKNOWLEDGMENTS

Financial support from the National Natural Science Foundation of China (Grant Nos. 52225406, 52073232, 52088101, and U1806219), the National Key Research and Development Program of China (Grant No. 2021YFB3700801), the Science Fund for Distinguished Young Scholars of Shaanxi Province (Grant No. 2020JC-11), and the Science Fund for Scientific and Technological Innovation Team of Shaanxi Province (Grant No. 2021TD-14), and discussions from Mr. K. L. Liu and Mr. B. Zhai are acknowledged.

AUTHOR DECLARATIONS

Conflict of Interest

The authors have no conflicts to disclose.

Author Contributions

R. L. Xiao: Conceptualization (equal); Formal analysis (equal); Investigation (equal); Methodology (equal); Writing – original draft (equal). **Q. Wang:** Formal analysis (supporting); Methodology (equal); Validation (equal). **J. Y. Qin:** Methodology (equal); Software (equal); Validation (equal). **J. F. Zhao:** Data curation (equal); Methodology (equal); Validation (equal). **Y. Ruan:** Conceptualization (equal); Funding acquisition (equal); Investigation (equal); Supervision (equal); Writing – review & editing (equal). **H. P. Wang:** Methodology (equal); Resources (equal). **H. Li:** Methodology (equal); Resources (equal). **B. Wei:** Funding acquisition (equal); Resources (equal); Supervision (equal); Writing – review & editing (equal).

DATA AVAILABILITY

The data that support the findings of this study are available from the corresponding author upon reasonable request.

REFERENCES

- ¹M. Lerbinger, A. Barbot, D. Vandembroucq, and S. Patinet, *Phys. Rev. Lett.* **129**, 195501 (2022).
- ²V. V. Karasiev, J. Hinz, S. X. Hu, and S. B. Trickey, *Nature* **600**, E12 (2021).
- ³O. G. Shpyrko, R. Streitel, V. S. K. Balagurusamy, A. Y. Grigoriev, M. Deutsch, B. M. Ocko, M. Meron, B. Lin, and P. S. Pershan, *Science* **313**, 77, (2006).
- ⁴A. Dobosz, Y. Plevachuk, V. Sklyarchuk, B. Sokoliuk, and T. Gancarz, *Int. J. Heat Mass Transfer* **126**, 414 (2018).
- ⁵A. K. Gangopadhyay, M. E. Blodgett, M. L. Johnson, A. J. Vogt, N. A. Mauro, and K. F. Kelton, *Appl. Phys. Lett.* **104**, 191907 (2014).
- ⁶R. L. Xiao, Y. Ruan, M. J. Lin, J. Y. Qin, H. Li, L. Hu, and B. Wei, *Sci. China Technol. Sci.* **64**, 2200 (2021).
- ⁷M. Mohr, R. Wunderlich, R. Novakovic, E. Ricci, and H. J. Fecht, *Adv. Eng. Mater.* **22**, 2000169 (2020).
- ⁸Q. Wang, B. Zhai, H. P. Wang, and B. Wei, *J. Appl. Phys.* **130**, 185103 (2021).
- ⁹M. K. Gupta, S. Kumar, R. Mittal, and S. L. Chaplot, *Phys. Rev. B* **106**, 014311 (2022).
- ¹⁰L. F. Zhang, J. Q. Han, H. Wang, R. Car, and W. N. E. Weinan, *Phys. Rev. Lett.* **120**, 143001 (2018).
- ¹¹H. Wang, L. F. Zhang, J. Q. Han, and W. N. E. Weinan, *Comput. Phys. Commun.* **228**, 178 (2018).
- ¹²R. E. Ryltsev and N. M. Chitchev, *J. Mol. Liq.* **349**, 118181 (2022).
- ¹³I. A. Balyakin, S. V. Rempel, R. E. Ryltsev, and A. A. Rempel, *Phys. Rev. E* **102**, 052125 (2020).
- ¹⁴C. Malosso, L. F. Zhang, R. Car, S. Baroni, and D. Tisi, *npj Comput. Mater.* **8**, 139 (2022).
- ¹⁵B. Zhai and H. P. Wang, *Comput. Mater. Sci.* **216**, 111843 (2023).
- ¹⁶H. Tang, Y. Zhang, Q. J. Li, H. W. Xu, Y. C. Wang, Y. Z. Wang, and J. Li, *Acta Mater.* **238**, 118217 (2022).
- ¹⁷X. Y. Wang, Y. N. Wang, L. F. Zhang, F. Z. Dai, and H. Wang, *Nucl. Fusion* **62**, 126013 (2022).
- ¹⁸G. Kresse and J. Furthmüller, *Phys. Rev. B* **54**, 11169 (1996).
- ¹⁹S. Plimpton, *J. Comput. Phys.* **117**, 1 (1995).
- ²⁰H. P. Wang, J. Chang, and B. Wei, *J. Appl. Phys.* **106**, 033506 (2009).
- ²¹M. J. P. Nijmeijer, A. F. Bakker, and C. Bruin, *J. Chem. Phys.* **89**, 3789 (1988).
- ²²Y. Zhang, A. Otani, and E. J. Maginn, *J. Chem. Theory Comput.* **11**, 3537 (2015).
- ²³T. Ishikawa, P. F. Paradis, J. T. Okada, and Y. Watanabe, *Meas. Sci. Technol.* **23**, 025305 (2012).
- ²⁴I. Egry, *Scr. Metall. Mater.* **28**, 1273 (1993).
- ²⁵M. I. Mendelev and M. J. Kramer, *J. Appl. Phys.* **107**, 073505 (2010).
- ²⁶S. P. Pan, S. D. Feng, J. W. Qiao, X. F. Niu, W. M. Wang, and J. Y. Qin, *Phys. Chem. Chem. Phys.* **19**, 22094 (2017).